TECHNICAL MEMORANDUM

677

Atmospheric Motion Vectors from model simulations. Part I: Methods and characterisation as single-level estimates of wind

A. Hernandez-Carrascal, N. Bormann,
R. Borde[1], H.-J. Lutz[1]
J. Otkin[2] and S. Wanzong[2]

Research Department

[1]EUMETSAT, Darmstadt, Germany
[2]CIMSS, Univ. of Wisconsin Madison, Madison, Wisconsin, USA

October 2012

Abstract

The main objective of the study described here is to improve the characterization of Atmospheric Motion Vectors (AMVs) and their errors to improve the use of AMVs in Numerical Weather Prediction (NWP). AMVs are estimates of atmospheric wind derived by tracking apparent motion across sequences of meteorological satellite images, and it is known that they tend to exhibit considerable systematic and random errors and geographically varying quality, as shown in comparisons against radiosonde or NWP data. However, there is a rather limited knowledge of the characteristics and origin of these errors: they can arise in the AMV derivation process, but they can also arise from the interpretation of AMVs as single-level point observations of wind. An important difficulty in the study of AMV errors is the scarcity of collocated observations of clouds and wind.

To overcome that difficulty, this study approaches the analysis of AMV errors using a simulation framework: geostationary imagery is generated from a high resolution NWP model simulation, and AMVs are derived from sequences of these simulated images. The NWP model provides the "truth" with a sophisticated description of the atmosphere on a high-resolution grid at frequent timesteps, which allows a detailed study of AMV errors, bypassing the usual difficulty of the scarcity of observations. Provided model simulations are realistic, the analysis of AMV errors in this setting can shed light on the nature of AMVs derived from observed imagery and their errors. The study is performed on the basis of Meteosat-8 simulations from the Weather Research and Forecasting (WRF) regional model, run with a nominal horizontal resolution of 3 km. SEVIRI channels IR10.8 and WV6.2 are used for the derivation of AMVs, and only AMVs obtained from cloudy scenes are used.

The study is described in two companion papers. The first part of the study is described here, and its key results are: 1) cloud structures in the WRF simulated imagery are generally realistic, although there are some unrealistic aspects during the first part of the study period, likely related to the spin-up, 2) the statistics comparing AMVs derived from WRF simulated imagery with the WRF true wind show characteristics that are broadly similar to statistics comparing real AMVs and NWP short-term forecasts, although differences appear to be larger, and 3) there is evidence for significant spatial, temporal and vertical error correlations, with the scales for the spatial error correlations broadly matching similar estimates for real data; for temporal and vertical error correlations, the current estimates are the first available, and they provide new insight with potential relevance to the specification of temporal thinning scales or observation error specifications in the assimilation. The second paper focusses on observation operator aspects.

1 Introduction

Atmospheric Motion Vectors (AMVs) derived from images from geostationary or polar satellites have long been an established ingredient to global and regional assimilation systems for Numerical Weather Prediction (NWP). Currently, AMVs largely provide the only source of upper level wind observations over the oceanic areas. The winds are derived by tracking targets such as clouds or water-vapour structures across image sequences (e.g. Nieman et al., 1997; Velden et al., 1997; Schmetz et al., 1993; Holmlund, 2000). An estimate of the appropriate height or pressure level is also provided by the winds producers, and this estimate is mostly based on an estimate of the cloud top (for high level winds) and the cloud base (for low-level winds).

In assimilation systems, NWP centres currently interpret AMVs as single-level point observations of the ambient wind. The AMVs are assimilated subject to strict quality control. The strict quality control is necessary as AMVs tend to exhibit considerable systematic errors and geographically varying quality, as shown in comparisons against radiosonde or model data (e.g. Bormann et al., 2002; Cotton and Forsythe, 2010). Winds producers also apply some quality control and provide guidance for the quality control through the provision of quality indicators (Holmlund, 1998; Rohn et al., 2001).

In recent years, further progress on the improved use of AMVs in assimilation systems has been hampered, for instance, due to a limited knowledge of the detailed error characteristics (systematic and random) and the origin of these errors. Errors can arise in the wind derivation, for instance from the recognised difficulties of assigning an appropriate height or from incorrect tracking, etc. But they can also arise from the use of non-passive tracers in the tracking step or the interpretation of AMVs as single-level point observations of wind. Study of these aspects with real data is often difficult due to a lack of detailed collocated observations of both wind and clouds.

In the current study we use a simulation framework, in which AMVs are derived from synthetic satellite images computed from an NWP model simulation. Here, the model simulation serves as truth and provides complete knowledge of the atmospheric structure that led to the derived AMV field, including the detailed distribution of clouds. Similar approaches have been used in the past, for instance to understand characteristics of clear-sky water vapour winds (Kelly et al., 1998), to investigate cloudy AMVs (von Bremen, 2008), or to test new AMV algorithms for future satellite instruments (Wanzong et al., 2008).

Our study is a follow-on from von Bremen (2008) who also used the simulation framework to better understand the characteristics of AMVs by comparing the derived AMVs against the model truth. Their work was based on sequences of Meteosat-8 images simulated from a 10-km resolution forecast from the ECMWF global model (in clear and cloudy conditions). These sequences were processed by CIMSS to derive AMVs. The analysis of the derived AMVs showed that the simulated AMVs exhibited a number of characteristics commonly found in monitoring statistics of real AMVs against short-term forecasts. The study focussed on the performance of quality control procedures, and the characteristics of the AMVs in some situations with known problems for real AMVs. There were indications that the extent of the tracked cloud in the vertical and the cloud evolution influence the quality of the derived AMV.

While the study of von Bremen (2008) provided a proof-of-concept, demonstrating the usefulness of the method for the characterisation of current AMVs, it also raised questions in a number of areas that required further study. Firstly, the study period was limited (6 hours), therefore limiting the sample size and representativity, and a longer study period would clearly be desirable. Secondly, the spatial model resolution was still coarser than that of today's geostationary imagers (3 to 4 km at nadir), leading to smoother images, the effect of which on the winds derivation is unclear. Thirdly, while the simulated images generally appeared realistic, no attempt was made to assess how well the model simulations and in particular the simulated images resemble reality, especially in terms of the represented cloud structures.

In the present study, the model used for the simulation is the Weather Research and Forecasting (WRF) regional model, run with a nominal horizontal resolution of 3 km, and the study period is 24 hours, therefore significantly improving on the spatial resolution and the length of the study period. The simulation is again performed for the Spinning Enhanced Visible and Infrared Imager (SEVIRI) instrument on board Meteosat-8, the Meteosat Second Generation geostationary satellite (e.g. Schmetz et al., 2002) located at $0°$ longitude at the time of the model simulation.

Section 2 describes the main characteristics of the model used in the simulation, the method used to generate simulated images, and the derivation system used to produce AMVs from the simulated imagery. In section 3, cloud structures from observed and simulated images are compared; this is an important step as findings from simulated imagery can be extended to observed imagery only if the cloud structures produced from the model simulation are realistic. Section 4 presents a statistical evaluation of AMVs, interpreted as single-level point estimates of wind, by comparing them against the model truth. In section 5, the horizontal, vertical and temporal correlations of errors are analyzed. Finally, section 6 concludes the report, summarizing the main findings and pointing at directions for further research. A companion paper (Hernandez-Carrascal and Bormann, 2012) focusses on observation operator aspects.

2   Model data, simulated images and AMV derivation

This study uses a simulation performed with the Weather Research and Forecasting (WRF) regional model (Skamarock et al., 2005), and covers the 24-hour study period starting on 16 August 2006 at 00 UTC. A second simulation was carried out, using the ECMWF global model with a nominal horizontal resolution of 10 km, mainly with the purpose of studying the sensitivity of the results to the model representation of the atmosphere, and in particular to the horizontal resolution of the underlying atmospheric model. Unfortunately the derived AMVs showed severe artefacts, and the analysis of the results was not continued. It appears that for the AMV derivation algorithm used in the current study, the 10 km spatial model resolution was not sufficient to produce meaningful results.

2.1   WRF simulation

The model fields from an existing simulation with the WRF regional model were obtained from CIMSS. The model simulation is described in Otkin et al. (2009) who also produced SEVIRI images from this simulation, albeit only half-hourly. The WRF is a compressible non-hydrostatic regional NWP model, further described in Skamarock et al. (2005). The dataset was produced with version 2.2 of the WRF, run over a domain covering the prime Meteosat disk (within 58.8° latitude), with a resolution that varies from 3 km at the equator to 1.7 km at the northern and southern boundaries. The simulation employed 52 levels in the vertical, with a model top located at 28 hPa. The WRF was initialised on 15 August 2006 18Z, from 1° analyses taken from the Global Data Assimilation System (GDAS). The study period is covered through a 6-30 h forecast, i.e. the spin-up period allowed to develop fine-scale structures from a coarser resolution initialisation analysis is 6 hours. We obtained the full model output every 15 min during the study period.

The WRF includes various microphysical quantities as prognostic variables. These are parameterized using the Thompson et al. (2008) mixed-phase cloud microphysics scheme. The simulation also employed the Mellor-Yamada-Janjic planetary boundary layer scheme (Mellor and Yamada, 1982). No cumulus parameterization was used - and any clouds were explicitly predicted by the microphysics scheme. Given the grid resolution, this means some small-scale convection will be absent from our simulations.

2.2   Radiative transfer simulation

The SEVIRI images for the WRF dataset were simulated every 15 min over the study period using version 9 of the RTTOV radiative transfer package (Saunders et al., 2008), following Chevallier and Kelly (2002). All 8 infrared and near-infrared channels of SEVIRI were simulated over the prime Meteosat disk (except for areas north of 58N and south of 58S for WRF due to the limited area domain). Solar effects were neglected for all simulated channels. Ocean surface emissivities were modelled using ISEM (Sherlock, 1999), whereas the land surface emissivity was set to 0.99 over moist and 0.93 over dry land, with no variation by channel. The WRF simulation was complemented with data from the ECMWF simulation mentioned earlier above the WRF model top (28 hPa). To mimick the SEVIRI viewing geometry, brightness temperatures (BTs) were calculated from a weighted spatial average of the relevant full resolution atmospheric model profiles and surface parameters for each SEVIRI pixel. Instrument noise has not been simulated for the images, as our aim is to characterise the errors arising in the processing and the interpretation of AMVs.

Cloud contributions in RTTOV are modelled through a multi-stream scattering parameterisation as de-

scribed in Matricardi (2005). The parameterisation uses layer values of cloud fraction, cloud liquid water and cloud ice. The ice water content is converted into a distribution of the effective diameters of ice particles using the model of McFarquhar et al. (2003) and the assumed shape of the ice crystals is aggregates. The WRF simulation output provides detailed information on microphysical species, but for the purpose of using RTTOV, these were combined into one liquid cloud category and one ice cloud category, the latter being a combination of all ice hydrometeors available from WRF. Cloud fraction was calculated from the spatial weighting of atmospheric profiles, assuming a cloud fraction of 1 for each contributing model grid point where some cloud is present.

2.3   AMV derivation

AMVs were derived by EUMETSAT from the WRF simulated imagery (SEVIRI channels IR10.8 and WV6.2), using a prototype derivation system developed in preparation for Meteosat Third Generation imagery (Borde et al., 2011) with some differences with respect to the one currently used by EUMETSAT operations (Schmetz et al., 1993; Holmlund, 2000).

The starting point is a triplet of consecutive images, with an interval of 15 minutes between them. Cross-correlation is used for the tracking step, and the CCC (Cross-Correlation Contribution) method is used to determine the feature tracked within each tracer box, and therefore to assign both height and horizontal location to each motion vector, effectively linking the tracking and the height assignment steps (Borde and Oyama, 2008). An estimate of the cloud top pressure for individual pixels within each tracked feature is obtained from the CLA (Cloud Analysis) product. This step makes use of atmospheric background information of temperature and humidity, usually obtained from a short-term forecast. In our case, the model truth was used in this step, with the WRF simulation subsampled to 2.5° spatial resolution required by the EUMETSAT processing algorithm. Note that this choice of background data eliminates errors arising from forecast errors in the background data. An automatic model-independent quality index is calculated for each AMV, combining several indices (measuring speed, direction, vector and spatial consistencies), following Holmlund (1998). The final QI is the product of a weighted sum of these consistency indices (with respective weights 1, 1, 1, and 2) and a pressure quality flag (Borde, personal communication).

3   Cloud structures comparison

In this section we present a comparison of the general cloud structures in the set of WRF simulated images and the real Meteosat-8 images. For the purpose of this study, we need to assess the realism of the image simulations, in particular in terms of the effective resolution and variability, as these will have an impact on the characteristics of the AMVs generated. Findings from simulated imagery can only be extended to observed imagery if the cloud structures produced from model simulations are realistic. From the perspective of this study, the quality of the two forecasts in the traditional sense is relatively unimportant. It is not necessary that the forecasts agree well with the observed images for a given time and place; in particular, location errors in the forecasts (e.g. misplacements of weather systems) are of no relevance, as the simulated atmospheres will serve as truth throughout the study. What is important is that the general appearance and variability of cloud structures in the simulated imagery agree well with the observed imagery.

3.1   Visual comparison of images

The visual comparison of simulated and observed images provides a useful first impression about cloud structures and some qualitative characteristics of the two sets of images. Figures 1 and 2 show examples of simulated and observed images at the beginning and end of the study period, for the SEVIRI channels IR10.8 and WV7.3. Several points are immediately apparent:

- At the end of the study period (right columns), the images from the WRF simulation show a generally realistic level of spatial detail and cloud distributions. While some cloud systems are represented differently or misplaced in the simulations compared to the observations, they nevertheless appear reasonable, even though the marine stratocumulus areas seem somewhat too noisy.

- At the beginning of the study period the extent of cirrus clouds appears overestimated and some clouds lack spatial variability. A likely reason for these features is that the WRF simulation seems to be still developing fine-scale structures during the early hours of our study period, i.e. the 6-hour spin-up allowed before our study period appears not to be sufficient. The spin-up is particularly severe as the simulation was initialised from comparatively coarse resolution analyses (at $1°$ resolution). Similar findings were reported by Otkin et al. (2009) in their investigation of imagery derived from this simulation. A visual inspection of the imagery suggests that these effects are noticeable for around the first 9 hours of the study period.

3.2   Frequency distributions of brightness temperatures

We will now aim to quantitatively summarise some of the characteristics of the simulated images. Figure 3 shows the frequency distribution of brightness temperatures (BT) for five SEVIRI channels, while Figure 4 shows the evolution of the frequency distributions throughout the study period; they show complementary descriptions of the distribution of clouds and humidity structures in the vertical. For both figures, the data taken into account in the calculations are all the pixels within the common WRF / Meteosat-8 area and with a satellite zenith angle less than $70°$, from images for all the timesteps in the study period.

For the longwave infrared channels ($10.8\,\mu m$ to $13.4\,\mu m$), the BT histograms shown in Figure 3 agree well between the WRF and the observed images, with a similar dynamic range and similar shape of the histograms. Some adjustments in the BT distributions are noticeable during the first 9-12 h of the simulation, related to the overestimation of cirrus clouds during the spin-up phase noted earlier (Figure 4). The diurnal skin temperature cycle over land leads to the increased frequencies for the highest brightness temperatures around the centre of the period, originating from cloud-free areas. These are captured similarly in the WRF and the observed dataset, albeit with a slightly larger dynamic range in the observed imagery.

For water vapour channels $6.2\,\mu m$ and $7.3\,\mu m$, the overall shapes of the BT distribution curves shown in Figure 3 are again similar for WRF and observed images, although the WRF distribution shows a cold bias with respect to the observed images, more noticeable with the $6.2\,\mu m$ channel, which peaks higher than the $7.3\,\mu m$ channel. This bias is probably related to an overestimation of water vapour in the upper troposphere in the WRF initialization dataset, as already reported in Otkin et al. (2009). As can be seen in Figure 4, the bias is strongest during the first 9-12 h of the study period, as the model adjusts to more realistic levels during its spin-up phase.

3.3 Spatial and temporal variability

Figure 5 shows maps depicting the standard deviation of the time series of BT for each pixel in the common WRF / Meteosat-8 area with a satellite zenith angle smaller than 70°. The figure includes maps for the SEVIRI channels IR10.8 and WV6.2, for observed and WRF sets of images. The time interval between images in the time series is 30 minutes, i.e. only alternate timesteps have been selected for the time series.

As shown in Figure 5, WRF and observed images are quite similar overall regarding temporal variability, for the SEVIRI channels IR10.8 and WV6.2. The maps show a comparable level of temporal variability in all areas, and in particular over the Intertropical Convergence Zone, although there are differences regarding e.g. the locations of the maxima of standard deviation, where deep convection and clear or low cloud skies alternate.

The effective resolution or spatial variability of the images has also been characterised, as this is of relevance to the success of the AMV tracking algorithm. The measure of the effective resolution follows the approach previously used by Chevallier and Kelly (2002), and it is defined as follows: for each pixel, we determine the smallest distance at which the correlation between the time series of brightness temperatures of a given pixel and those of all other pixels drops below a given threshold. That is, the measure quantifies the scales at which the brightness temperature shows significant variability. After some experimentation we chose 0.9 as the correlation threshold; lower values tend to lead to larger estimates of the effective resolution, but qualitatively similar results. Note that here the effective resolution is calculated on a pixel-by-pixel basis over one-day time-series of brightness temperatures, whereas Chevallier and Kelly (2002) considered larger spatial averages over a much longer period. Our estimates of the effective resolution are therefore not comparable to those of Chevallier and Kelly (2002).

Given that our time-series are relatively short, we found that the pixel-by-pixel estimates of the effective resolution depend on the standard deviation of the brightness temperatures for the given pixel over the study period. Pixels with low standard deviations lead to unreliable estimates of the effective resolution, as the calculation involves the division by a value close to 0. We hence present our results in terms of 2-dimensional histograms of the number of pixels exhibiting a certain standard deviation and effective resolution, excluding cases with too low standard deviations.

In Figure 6, the WRF images show effective resolution/standard deviation relationships that compare well with those obtained from the observed images. Both show effective resolution peaks in the 2-dimensional histograms around 10-15 km. This further demonstrates that the spatial variability of the clouds represented in the WRF imagery is overall consistent with the observed images.

4 Statistical evaluation of single-level AMVs versus model truth

In this section, we present an evaluation of the AMVs derived from WRF simulated images, comparing them with the truth provided by the model simulations, following the traditional interpretation of AMVs as single-level point estimates of wind. To assess the impact of the spin-up noted earlier for the first 9-12 h of the study period, some of the presented statistics have been calculated separately for the first and the second half of the study period. The differences for the two periods were relatively small, suggesting that the spin-up has only a small effect on the AMV quality characteristics.

In all the statistical comparisons presented in this section, only AMVs with a model-independent quality index $QI > 80\%$ were considered. Although it is possible to produce clear-sky AMVs from WV6.2

imagery by tracking moisture patterns, only cloudy AMVs were produced for this study; therefore all AMVs in this study have been obtained by tracking clouds as determined in the EUMETSAT cloud analysis from the imagery. The (true) model wind was calculated in the following way: for each AMV, from its horizontal coordinates, vertical profiles of u and v from the model at the nearest gridpoint were obtained, and the model wind (u, v) was calculated by linear interpolation of these two profiles to the original AMV pressure, i.e. the one assigned to the AMV during the derivation process.

Throughout the study, the classification of AMVs according to vertical level and to latitude band is the usual in the AMV community, and as recommended by the Working Group on Verification Statistics in the Third International Winds Workshop (EUMETSAT, 1996):

- AMVs are classified according to their assigned pressure as low-level (> 700 hPa), medium-level (between 700 and 400 hPa) and high-level (< 400 hPa).

- Three latitude bands are considered: northern hemisphere extra-tropics (north of 20N), tropics (20S to 20N) and southern hemisphere extra-tropics (south of 20S).

In the following, we compare the statistics for the WRF-derived AMVs against those obtained from observed images at EUMETSAT operations at the time (16 August 2006). The latter are compared against short-term operational forecasts from ECMWF's global assimilation system, to provide a reference for the statistics derived from the simulated AMVs. Note that the comparison between the real AMVs and the ECMWF short-term forecasts include a component of forecast error, whereas that is eliminated by design in the comparisons between simulated winds and the model truth.

Ideally, the AMVs from observed images should have been generated by the same derivation system that was used for the WRF imagery, but unfortunately such AMVs were available only for four timesteps, which is too small a sample to allow meaningful comparisons. As described in section 2.3, there are differences between the prototype derivation algorithm used in this study and the algorithm used in operations at the time. In particular, the use of the CCC method has important implications regarding height assignment. Less obvious, but also important, are the differences regarding quality control. Although the QI threshold used for statistics is 80% for both AMV datasets and the principles behind the calculation of the QIs are essentially the same, the prototype derivation algorithm also includes a pressure quality flag, and the weights given to different QI components may be different; the consequence is that the final QIs may differ considerably. Note also that the WRF-simulated AMVs were available half-hourly, whereas the operational AMVs at the time were produced hourly, therefore we expect around half the number of AMVs to be available from operations over the study day. As the sampling is homogeneous during the day, we do not expect this sampling effect to affect our statistics in a significant way.

Table 1 and Figures 7 and 8 show the standard statistics for high-level AMVs derived from the WRF WV6.2 imagery and from EUMETSAT operations at the time. A slow bias is apparent for the three latitude bands, particularly for the southern hemisphere extra-tropics. The biases seen here for the WRF dataset are larger than those for the observed AMVs for the same day (e.g., Table 1). However, slow biases are a common feature for high level AMVs, and the magnitude of the biases seen here are within what is commonly seen in comparisons between AMVs and radiosondes or model data over different periods. Figure 7 shows that for the extra-tropics the bias is caused by a general shift towards slower AMV speeds, rather than by a large number of outliers. In contrast, outliers appear more common for the WRF AMVs in the tropics. Similarly, the root mean squared vector differences (RMSVDs) are somewhat larger for the WRF AMVs than for the observed winds. The WRF dataset includes more AMVs than the operational one, as expected from the different temporal sampling, but in some areas there are less than twice the number of AMVs available from the WRF simulation.

Meteosat-8 WV6.2 AMVs - High level, QI $> 80\%$								
	Global		**NH**		**TR**		**SH**	
	WRF	**OPS**	**WRF**	**OPS**	**WRF**	**OPS**	**WRF**	**OPS**
Number	91993	57513	16499	10865	36289	25931	39205	20717
Speed bias [m/s]	-2.592	0.328	-2.729	0.095	-1.057	1.221	-3.955	-0.668
AMV speed [m/s]	25.37	24.57	21.25	22.24	13.80	12.74	37.81	40.60
RMSVD [m/s]	10.38	7.47	8.55	6.88	10.78	6.78	10.70	8.53
NRMSVD [m/s]	0.409	0.304	0.403	0.309	0.781	0.533	0.283	0.210

Table 1: Summary statistics for high-level AMVs derived from WRF simulated WV6.2 images (left column of each pair) and from operations at the time (right column). Only winds with a model-independent QI $> 80\%$ have been used.

Regarding direction, the general appearance of histograms for WRF AMVs and for AMVs from operations is similar (Figure 8). There seems to be a tendency for WRF AMVs to favour some directions, shown in the histograms as vertical lines. If we remember that only AMVs with $QI > 80\%$ have been taken into account for the statistics, a more accurate view is that a certain group of AMVs seems to be more likely to end with a high QI and to prefer certain directions. This tendency is not seen in the set of AMVs from operations, and further investigations suggest that it is a feature of the AMV derivation system used in this study, rather than the simulation approach.

Table 2 shows the standard statistics for AMVs derived from the WRF IR10.8 imagery and from EUMETSAT operations at the time. Here, there tend to be more than twice the number of winds available in the WRF dataset compared to OPS, possibly a result of different characteristics of the QI or other aspects in the processing. High-level AMVs show the same general characteristics as high-level AMVs from WV6.2 imagery, although the slow bias is more marked, and both RMSVD and the normalised RMSVD (ie normalised with the mean wind speed) are larger than with the WRF WV6.2 imagery, for the three latitude bands. Low-level WRF AMVs show a fast bias for tropics, and small slow biases for extra-tropics.

Figures 9 and 10 show, respectively, speed and direction histograms for low-level AMVs derived from the WRF IR10.8 images (left), and for AMVs derived from observed IR10.8 imagery by EUMETSAT operations at the time (right). Regarding speed (Figure 9), the two sets of AMVs display similar overall characteristics, although here are differences: speed biases are very small for the set from operations, while there is a clear fast bias in the tropics in the WRF set. Regarding direction (Figure 10), there seems to be a tendency for (high-QI) low-level AMVs to favour some directions, even stronger than with the set of high-level AMVs from the WRF WV6.2 images.

The finding that the WRF-simulated AMVs compare more poorly to the truth than the operational AMVs compare to short-term forecasts is to some extent unexpected, and may point to limitations of the simulation approach. The comparisons between operational AMVs and short-term forecasts include a component of forecast error, and hence would be expected to compare more poorly. One possible explanation is that this is due to a poorer performance of the EUMETSAT prototype system compared to operations at the time. However, by investigating the four time-slots for which AMVs derived from real imagery were available from the prototype system, we found that this is not the case. While the two systems produce AMVs with some different characteristics, the differences are smaller than those seen here between the WRF and OPS comparisons. The poorer statistics for the WRF-simulated AMVs are hence likely due to limitations in the simulation approach or in this specific simulation, for instance due to a poorer performance of the height assignment or the tracking step. This aspect has to be kept in mind

Meteosat-8 IR10.8 AMVs - High level, QI > 80%							
	Global		NH		TR		SH	
	WRF	OPS	WRF	OPS	WRF	OPS	WRF	OPS
Number	115322	42046	22962	9301	45360	17270	47000	15475
Speed bias [m/s]	-4.801	-0.698	-4.718	-0.488	-2.611	0.035	-6.956	-1.642
AMV speed [m/s]	22.70	23.26	19.29	20.97	11.98	11.37	34.72	37.90
RMSVD [m/s]	12.76	7.16	10.12	6.16	11.70	5.99	14.75	8.75
NRMSVD [m/s]	0.562	0.308	0.525	0.294	0.977	0.526	0.425	0.231

Meteosat-8 IR10.8 AMVs - Mid level, QI > 80%							
	Global		NH		TR		SH	
	WRF	OPS	WRF	OPS	WRF	OPS	WRF	OPS
Number	29832	7886	5293	1630	14654	2900	9885	3356
Speed bias [m/s]	-2.547	-0.748	-3.420	-0.238	1.530	1.208	-8.124	-2.687
AMV speed [m/s]	11.69	17.04	12.26	12.38	8.05	8.51	16.77	26.68
RMSVD [m/s]	9.41	6.77	6.64	4.60	6.70	4.39	13.31	8.98
NRMSVD [m/s]	0.805	0.397	0.542	0.372	0.833	0.516	0.794	0.337

Meteosat-8 IR10.8 AMVs - Low level, QI > 80%							
	Global		NH		TR		SH	
	WRF	OPS	WRF	OPS	WRF	OPS	WRF	OPS
Number	125504	51641	8555	4648	84298	33982	32651	13011
Speed bias [m/s]	1.036	0.053	-0.391	0.177	1.592	-0.041	-0.025	0.254
AMV speed [m/s]	9.05	9.13	8.50	10.54	9.01	8.75	9.27	9.62
RMSVD [m/s]	4.79	3.28	3.43	3.85	4.99	3.45	4.56	2.55
NRMSVD [m/s]	0.530	0.360	0.403	0.365	0.554	0.394	0.492	0.265

Table 2: Summary statistics for AMVs derived from WRF simulated IR10.8 images (left column of each pair) and from operations at the time (right column). Only winds with a model-independent QI > 80% have been used.

when interpreting the results from this assimilation study, and we get back to this point in the companion paper (Hernandez-Carrascal and Bormann, 2012).

Despite these caveats, our analysis suggests that the WRF AMVs are qualitatively broadly in line with characteristics commonly found in comparisons of real AMVs with short-term forecasts. In particular, slow biases prevail in the extra-tropics at high levels and fast speed biases are present at mid-levels in the tropics - features commonly observed in real AMVs.

5 Error correlations from simulated AMVs

Error correlations between different AMVs are an unavoidable feature, as errors in the height assignment, the background data used in the winds derivation, the interpretation of the AMVs, the quality control or the spatial representativeness may all be correlated spatially, vertically, or temporally. For instance, Bormann et al. (2003) investigated spatial error correlations in real AMVs, and found significant correlations on scales of several hundreds of kilometres, with broader correlations over the tropics than over the extra-tropics. Similar findings have been reported by Berger et al. (2006) and Bonavita and Torrisi (2006). To our knowledge, temporal or vertical error correlations for real AMVs have not yet been quantified.

Knowledge about error correlations is relevant to the assimilation of AMVs, as the presence of error correlations affects important data assimilation parameters such as the setting of observation errors and data selection/thinning scales. Currently, the operational assimilation of AMVs neglects error correlations, and uses instead inflated observation errors. However, Isaksen and Radnoti (2010) developed methods to take some of the effects of error correlations explicitly into account in data assimilation, and applied these to AMVs with mixed success. Experimentation with error correlations would be helped by a better specification of the correlation scales, especially for vertical and temporal error correlations.

5.1 Method

Here we calculate spatial as well as temporal and vertical error correlations from the simulated AMVs. This calculation is straightforward in the simulation framework, as the differences between AMVs and the model truth are readily available. As in the previous section, we treat the AMVs as single-level point measurements. Also, throughout this investigation a QI threshold of 80% has been applied to screen out poor-quality AMVs and WV AMVs with an assigned pressure larger than 700 hPa were ignored.

The calculations are based on a set of pairs of differences between AMVs and the model truth. This set has been produced by pairing up each simulated AMV with all available other AMVs (subject to certain criteria). Spatial, temporal, and vertical error correlations have been calculated by binning the AMV pairs into suitable spatial, temporal, and vertical distance intervals. For spatial correlations, only isotropic correlations are considered here, i.e. those which depend only on the distance between the two pairs. Large-scale geographical biases have been removed by subtracting the mean error for each geographical region/layer shown. Table 3 shows the criteria used to pair up and bin the AMVs, in order to focus on spatial, temporal, and vertical correlations.

	Criteria to match pairs	Binning interval
Spatial	Temporal: AMVs originate from the same triplet Vertical: less than 50 hPa apart	50 km
Vertical	Temporal: AMVs originate from the same triplet Spatial: less than 100 km apart	50 hPa
Temporal	Spatial: less than 100 km apart Vertical: less than 50 hPa apart	1/2 h

Table 3: Matching and binning parameters used to obtain the error correlation data.

As in Bormann et al. (2003), we will show only the average between the correlations for the u-component and the v-component. For spatial error correlations, an analytical function is fitted to the correlation relationship, primarily to aid the comparison to results presented in Bormann et al. (2003). As in Bormann et al. (2003), the chosen function is the Second Order Autoregressive (SOAR) function, with

$$R(r) = R_0 \left(1 + \frac{r}{L}\right) e^{-\frac{r}{L}} \tag{1}$$

Here, R_0 indicates the proportion of the spatially correlated part of the error, whereas L is a length scale. Note that for the chosen function $R(L) = 2R_0/e$, and not R_0/e as for many other correlation functions.

5.2   Results

The simulated AMVs show considerable error correlations, spatially, temporally, and vertically. We will quantify these in the following, giving results for both the IR and the WV channels.

Spatial error correlations for the simulated AMVs are shown in Figures 11 and 12. The error correlations appear broader in the tropics for both channels, and high level AMVs in the extra-tropics show the narrowest error correlations. The results are fairly similar for different levels in the vertical, but there is some suggestion that mid-level winds have broader error correlations in the extra-tropics than high level winds.

Qualitatively, these findings compare well with those of Bormann et al. (2003) who also found broader error correlations in the tropics for real AMVs, and relatively little variation in the vertical. To allow a more quantitative comparison, we also present the results from fitting the SOAR function to our correlation data. The fit has been calculated by minimising the sum of the squared differences, weighted by the number of AMV pairs available for each bin. The point at zero distance has been excluded, to allow for the possibility of a spatially uncorrelated error. It is apparent from Figures 11 and 12 that the fit of the SOAR function to the correlation data is not as good as it is in Bormann et al. (2003), especially for the southern hemisphere extra-tropics. This may be an artefact of the limited sampling, or it might suggest that the errors found here show a different spatial structure.

Table 4 shows the results from fitting the SOAR function, for comparison with Tables 2 and 3 in Bormann et al. (2003). Note that R_0 in Bormann et al. (2003) represented the spatially correlated part of AMV/radiosondes differences, whereas in our case it gives the actual proportion of the spatially correlated error, so the two values should not be compared. A strict comparison for L is also not possible, as Bormann et al. (2003) used a whole year of AMV data from all operational satellites at the time, and values for Meteosat-8 are therefore not provided. Nevertheless, there is reasonable agreement between our results and those for real data over the range of satellites, with values of 140-280 km for the extra-tropics in our case compared to values of around 150-260 km for the real data, and values of 315-490 km for the tropics compared to around 260-370 km for the real data. However, the values for the spatially correlated part of the error are much larger for the simulated AMVs than they are for the real data. This means it is not clear that the error correlations shown in our study originate from the same source as in the real data.

It is worth noting that the values for R_0 indicate the presence of a non-negligible error that is spatially uncorrelated (Table 4). Bormann et al. (2003) previously hypothesised that the uncorrelated error is small, and that almost all of the error in the AMVs is spatially correlated. For the simulated winds it appears that the spatially correlated error is indeed dominant, but the spatially uncorrelated part is nevertheless significant.

Temporal error correlations are shown in Figures 13 and 14. These are fairly broad, reaching values of

				IR winds						WV winds			
		R_0	$L\,[km]$	$\sigma_{cor}\,[m/s]$		$\sigma_{uncor}\,[m/s]$		R_0	$L\,[km]$	$\sigma_{cor}\,[m/s]$		$\sigma_{uncor}\,[m/s]$	
				u	v	u	v			u	v	u	v
NH	High lev	0.75	137	6.1	5.4	3.5	3.1	0.66	126	5.3	4.0	3.8	2.9
	Mid lev	0.84	151	4.0	3.7	1.7	1.6	-	-	-	-	-	-
	Low lev	0.71	152	1.9	1.9	1.3	1.2	-	-	-	-	-	-
TR	High lev	0.67	348	8.0	4.9	5.6	3.4	0.69	493	7.2	4.7	4.8	3.2
	Mid lev	0.76	356	4.1	3.5	2.3	2.0	-	-	-	-	-	-
	Low lev	0.70	348	2.7	2.6	1.8	1.7	-	-	-	-	-	-
SH	High lev	0.59	248	8.2	5.6	7.0	4.7	0.62	176	5.9	5.0	4.7	4.0
	Mid lev	0.80	277	7.5	5.0	3.7	2.5	-	-	-	-	-	-
	Low lev	0.82	215	3.0	2.8	1.4	1.3	-	-	-	-	-	-

Table 4: Fitting parameters obtained by fitting the SOAR function to the correlation data. Also shown are σ_{cor} and σ_{uncor}, the spatially correlated and uncorrelated part of the AMV error, for u and v, respectively. This has been obtained by partitioning the variance of the differences between AMVs and model truth at zero separation using the estimate of R_0.

0.2 at around 4-8 h for high level winds in the extra-tropics, and at around 15-20 h in the tropics. Over the southern hemisphere extra-tropics, low level IR winds show especially broad correlations, linked to persistent geographically varying biases for the low level winds. Similar to the spatial correlations, there are indications of a notable temporally uncorrelated error.

To our knowledge, these are the first estimates of temporal error correlations for AMVs; hence a comparison of findings with real AMVs is not possible. It is likely that the differences seen for the temporal correlations for geographical regions or layers are related to persistent height assignment errors combined with typical time-scales for the evolution of cloud fields. For instance, the low level IR winds for the southern hemisphere extra-tropics originate largely from persistent inversion clouds, contributing to broader temporal correlations. Such temporal error correlations are especially relevant in the context of the move towards hourly AMVs at various processing centres. Such error correlations are currently ignored in data assimilation systems, and may therefore negatively affect the impact of these AMVs.

Vertical correlations are shown in Figure 15. Here, we chose to combine the IR and WV winds, to improve the sample size available. Note that as only one AMV can be derived per segment from an image triplet from the same channel, the vertical error correlations are based on pairs of AMVs that are immediate neighbours or originate from different channels. In the vertical, error correlations reach values of 0.2 for separations of around 100-150 hPa. Again, these provide the first estimates of vertical error correlations for AMVs.

It should be kept in mind that the estimates for error correlations presented here are based on a single 24-hour period, and hence are based on a relatively limited sample. Also, the errors found for the simulated dataset are considerably larger than those commonly encountered for real AMVs, so the direct applicability of the results to real AMVs is not clear. Nevertheless, it is encouraging to see qualitative and quantitative agreement between our results and those for real data in terms of the error correlation scales

for spatial error correlations. This suggests that the findings for the simulated data are likely to provide some indication for the presence of temporal and vertical error correlations in real AMVs, at least in a qualitative sense. Such error correlations are very difficult to obtain for real data, and the simulation framework may well be the only practical way to shed some light on these.

6 Conclusions

This paper has presented the first part of a study whose main objective is to improve the understanding of the characteristics and origins of AMV errors, to improve the use of AMVs in Numerical Weather Prediction. Using a simulation framework, we have studied several aspects of AMVs and their errors.

Regarding the realism of cloud structures from simulated images, visual inspection and a statistical analysis of brightness temperatures have shown that the WRF simulated imagery is reasonably realistic. However, it is also clear that the simulation is still in a spin-up phase during the first part of the study period.

We have presented an evaluation of cloudy AMVs from WRF WV6.2 and IR10.8 simulated imageries, according to the traditional interpretation of AMVs as single-level point estimates of wind at the assigned pressure. The simulated AMVs show characteristics that are broadly similar to comparisons between real AMVs and short-term forecasts. However, errors in the simulated winds appear larger than those in the real data, so some care has to be taken when interpreting the results from this study for real data. As highlighted in our companion paper (Hernandez-Carrascal and Bormann, 2012), some of these poorer statistics may be related to systematic height assignment errors specific to the simulation. Also, experiments with AMVs derived from a lower-resolution simulation highlighted the importance of using a high-resolution model for AMV simulation studies; the 1.7-3 km dataset used here appears to be adequate.

The simulated AMVs show significant horizontal, temporal, and vertical error correlations when the AMVs are interpreted as single-level values. The horizontal error correlation scales obtained from the simulated dataset agree qualitatively well with similar estimates from real AMVs, with non-negligible error correlations for distances of around 300 km in the extra-tropics and even broader correlations in the tropics. For temporal and vertical error correlations, our analysis provide the first estimates of correlation scales, and we find non-negligible error correlations in the range of 6-12 h and 100 hPa, respectively. Such error correlations are currently neglected in today's assimilation systems, and this may limit or penalise their impact. Note, however, that the error estimates obtained in this study are larger than those found in studies with real data, so the direct applicability of the results to real data is not clear. Further investigations are possible with the simulated dataset, for instance, to investigate the origins of the correlated errors by using alternative AMV height interpretations.

The present paper has used AMVs in the traditional way, interpreting them as estimates of wind at a single level, assumed to be the top of the tracked cloud structure. In a companion paper (Hernandez-Carrascal and Bormann, 2012), we explore alternative interpretations of AMVs, making use of the detailed description of the atmosphere available in the simulation framework.

Acknowledgements

References

Berger, H., C. Velden, and J. LeMarshall (2006). New quality indicators for GOES derived winds and their potential effect on NWP data impact experiments. *Proceedings of the Eigth International Winds Workshop, Beijing, China, 24-28 April 2006*.

Bonavita, M. and L. Torrisi (2006). Characterization and use of MSG AMVs in the italian weather service regional NWP system. *Proceedings of the Eigth International Winds Workshop, Beijing, China, 24-28 April 2006*.

Borde, R. and R. Oyama (2008). A direct link between feature tracking and height assignment of operational Atmospheric Motion Vectors. *Proceedings of the Ninth International Winds Workshop, Annapolis, Maryland, USA, 14-18 April 2008*.

Borde, R., A. D. Smet, G. Dew, P. Watts, H.-J. Lutz, M. Carranza, and M. Doutriaux-Boucher (2011). AMV extraction scheme for MTG-FCI at EUMETSAT. *Proceedings of the 2011 EUMETSAT Conference, Oslo, Norway, 5-9 Sep 2011*.

Bormann, N., G. Kelly, and J.-N. Thépaut (2002). Characterising and correcting speed biases in Atmospheric Motion Vectors within the ECMWF system. *Proceedings of the Sixth International Winds Workshop, Madison, Wisconsin, USA, 7-10 May 2002*.

Bormann, N., S. Saarinen, G. Kelly, and J.-N. Thépaut (2003). The spatial structure of observation errors in atmospheric motion vectors from geostationary satellite data. *Mon. Wea. Rev. 131*, 706–718.

Chevallier, F. and G. Kelly (2002). Model clouds as seen from space: comparison with geostationary imagery in the 11μ window channel. *Mon. Wea. Rev. 130*, 712–722.

Cotton, J. and M. Forsythe (2010). NWP SAF AMV monitoring, 4th analysis report. The Met. Office, Exeter, United Kingdom. *Available online from: http://research.metoffice.gov.uk/research/interproj/nwpsaf/satwind_report/analysis.html*.

EUMETSAT (1996). Report from the Working Group on Verification Statistics. *Proceedings of the Third International Winds Workshop, Ascona, Switzerland, 10-12 June 1996*.

Hernandez-Carrascal, A. and N. Bormann (2012). Atmospheric Motion Vectors from model simulations. Part II: Interpretation as spatial and vertical averages of wind and role of clouds. *ECMWF Technical Memorandum No. 678*.

Holmlund, K. (1998). The utilization of statistical properties of satellite-derived atmospheric motion vectors to derive quality indicators. *Wea. Forecasting 13*, 1093–1104.

Holmlund, K. (2000). The Atmospheric Motion Vector retrieval scheme for Meteosat Second Generation. *Proceedings of the Fifth International Winds Workshop, Lorne, Australia, 28 Feb - 3 Mar 2000*.

Isaksen, L. and G. Radnoti (2010). Accounting for Atmospheric Motion Vector error correlations in the ECMWF 4D-VAR and ensembles of data assimilations. *Proceedings of the Tenth International Winds Workshop, Tokyo, Japan, 22-26 Feb 2010.*

Kelly, G., R. Munro, M. Rohn, and K. Holmlund (1998). Impact of Atmospheric Motion Vectors on the ECMWF system and the development of a water vapour AMV observation operator. *Proceedings of the Fourth International Winds Workshop, Saanenmöser, Switzerland, 20-23 October 1998.*

Matricardi, M. (2005). The inclusion of aerosols and clouds in RTIASI, the ECMWF fast radiative transfer model for the Infrared Atmospheric Sounding Interferometer. *ECMWF Technical Memorandum No. 474.*

McFarquhar, G. M., S. Iacobellis, and R. C. J. Somerville (2003). SCM simulations of tropical ice clouds using observationally based parameterizations of microphysics. *J. Climate 16*, 1643–1664.

Mellor, G. L. and T. Yamada (1982). Development of a turbulence closure model for geophysical fluid problems. *Rev. Geophys. Space Phys. 20*, 851–875.

Nieman, S. J., W. P. Menzel, C. M. Hayden, D. Gray, S. T. Wanzong, C. S. Velden, and J. Daniels (1997). Fully automated cloud-drift winds in NESDIS operations. *Bull. Amer. Meteor. Soc. 78*, 1121–1133.

Otkin, J. A., T. J. Greenwald, J. Sieglaff, and H.-L. Huang (2009). Validation of a Large-Scale Simulated Brightness Temperature Dataset Using SEVIRI Satellite Observations. *J. Appl. Meteor. Climatol. 48*, 1613–1626.

Rohn, M., G. Kelly, and R. Saunders (2001). Impact of a new cloud motion wind product from Meteosat on NWP analyses. *Mon. Wea. Rev. 129*, 2392–2403.

Saunders, R., M. Matricardi, P. Rayer, T. Blackmore, N. Bormann, D. Salmond, A. Geer, P. Brunel, and P. Marguinaud (2008). What can RTTOV-9 do for me? *Proceedings of the 16th international TOVS study conference, Angra dos Reis, Brazil, 7-13 May 2008.*

Schmetz, J., K. Holmlund, J. Hoffman, B. Strauss, B. Mason, V. Gaertner, A. Koch, and L. V. D. Berg (1993). Operational Cloud-Motion Winds from Meteosat Infrared Images. *J. Appl. Meteorol. 32*, 1206–1225.

Schmetz, J., P. Pili, S. Tjemkes, D. Just, K. Kerkmann, S. Rota, and A. Ratier (2002). An introduction to Meteosat Second Generation (MSG). *Bull. Amer. Meteor. Soc. 83*, 977–992.

Sherlock, V. (1999). ISEM-6: Infrared Surface Emissivity Model for RTTOV-6. *Forecasting Research Tech. Rep. FR-299, UK Met. Office, 17 pp.*

Skamarock, W. C., J. B. Klemp, J. Dudhia, D. O. Gill, D. M. Barker, W. Wang, and J. G. Powers (2005). A description of the Advanced Research WRF version 2. *NCAR Tech. Note TN-4681STR, 88 pp.*

Thompson, G., P. R. Field, R. M. Rasmussen, and W. Hall (2008). Explicit forecasts of winter precipitation using an improved bulk microphysics scheme. Part II: Implementation of a new snow parameterization. *Mon. Wea. Rev. 136*, 5095–5115.

Velden, C. S., C. M. Hayden, S. J. Nieman, W. P. Menzel, S. T. Wanzong, and J. S. Goerss (1997). Upper-tropospheric winds derived from geostationary satellite water vapor observations. *Bull. Amer. Meteor. Soc. 78*, 173–195.

von Bremen, L. (2008). Using simulated satellite images to improve the characterization of Atmospheric Motion Vectors (AMVs) and their errors for Numerical Weather Prediction. *NWP SAF report NWPSAF-EC-VS-015. Available from http://research.metoffice.gov.uk/research/ interproj/nwpsaf/vs.html*.

Wanzong, S., I. Genkova, C. Velden, and D. Santek (2008). AMV research using simulated datasets. *Proceedings of the Ninth International Winds Workshop, Annapolis, USA, 14-18 April 2008.*
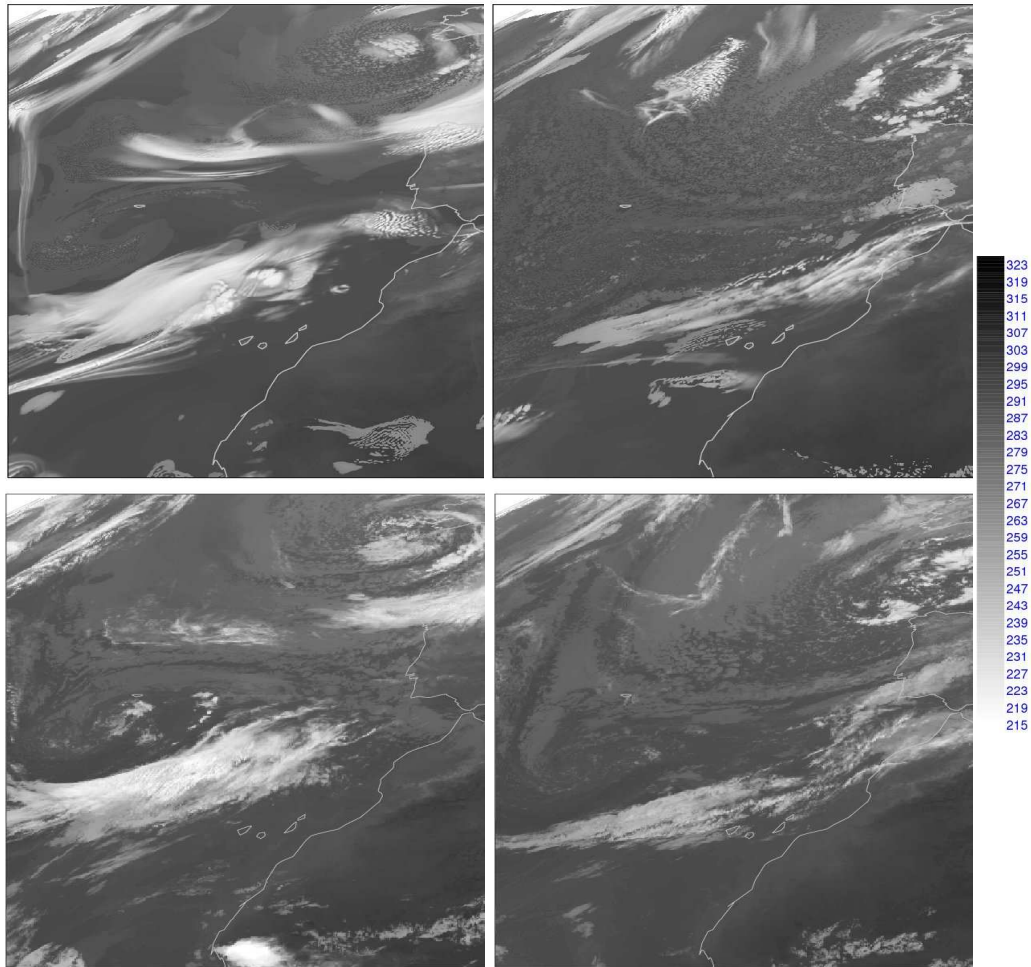
Figure 1: Simulated and observed satellite images [K] in the $10.8\,\mu m$ band of SEVIRI, zoomed over the eastern North Atlantic. The left column is for 00 Z on 16 August 2006 and the right column for 00 Z on 17 August 2006, i.e. respectively the beginning and the end of the study period. The top row shows WRF simulated images, and the bottom row observed images.

ECMWF

Atmospheric Motion Vectors from model simulations. Part I
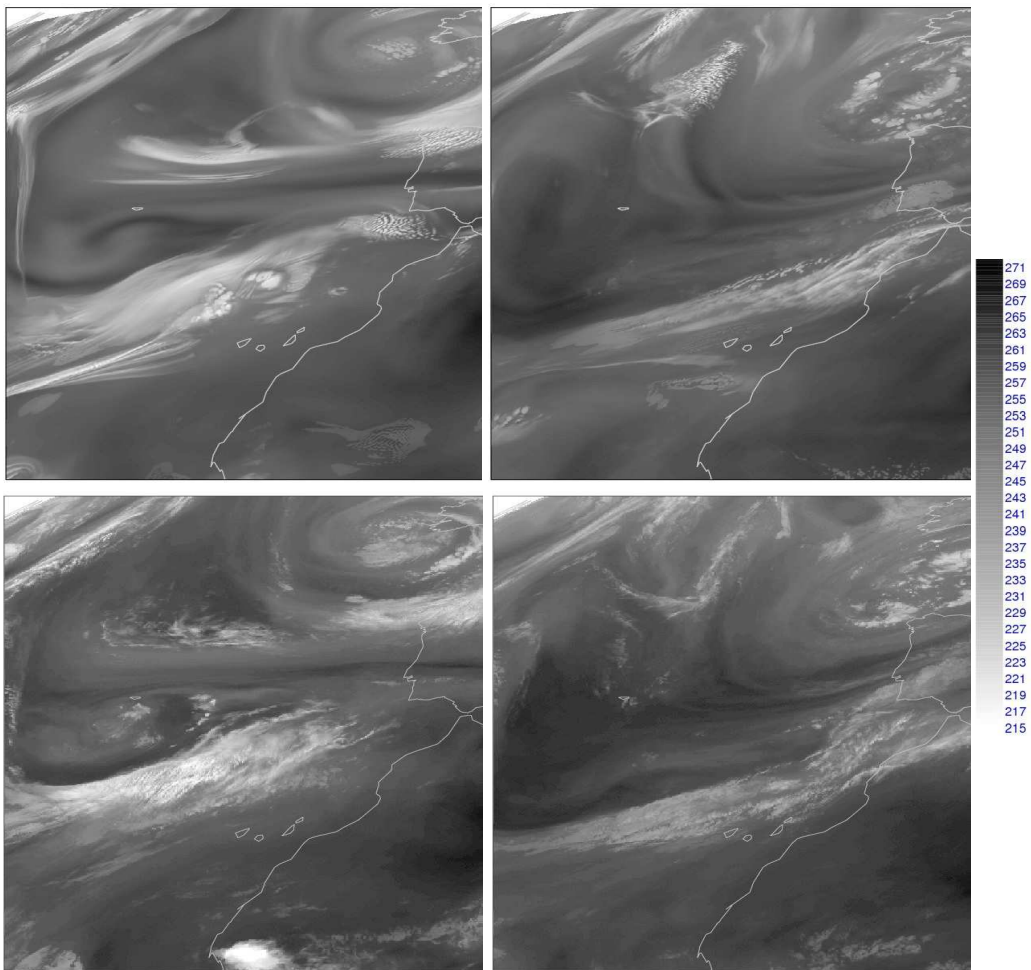
Figure 2: As Figure 1, but for the WV 7.3 µm.
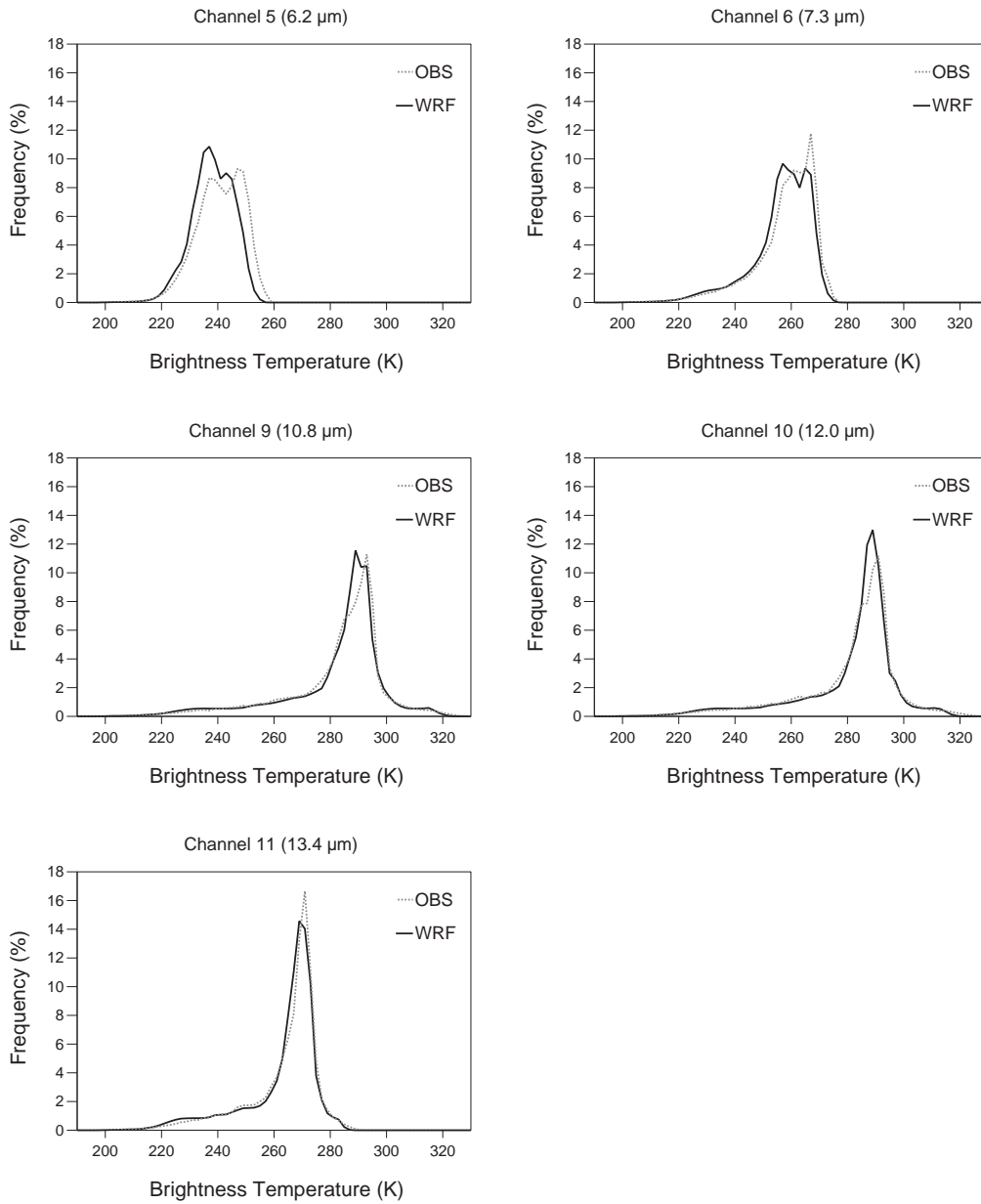
Figure 3: Frequency distribution of brightness temperatures for SEVIRI channels WV6.2, WV7.3, IR10.8, IR12.0 and IR13.4 for observed and WRF images. The bin size used is 2K. All the timesteps in the study period, and all the pixels with a satellite zenith angle less than 70°, *within the WRF latitude range, have been taken into account in the statistics.*

ECMWF

Atmospheric Motion Vectors from model simulations. Part I
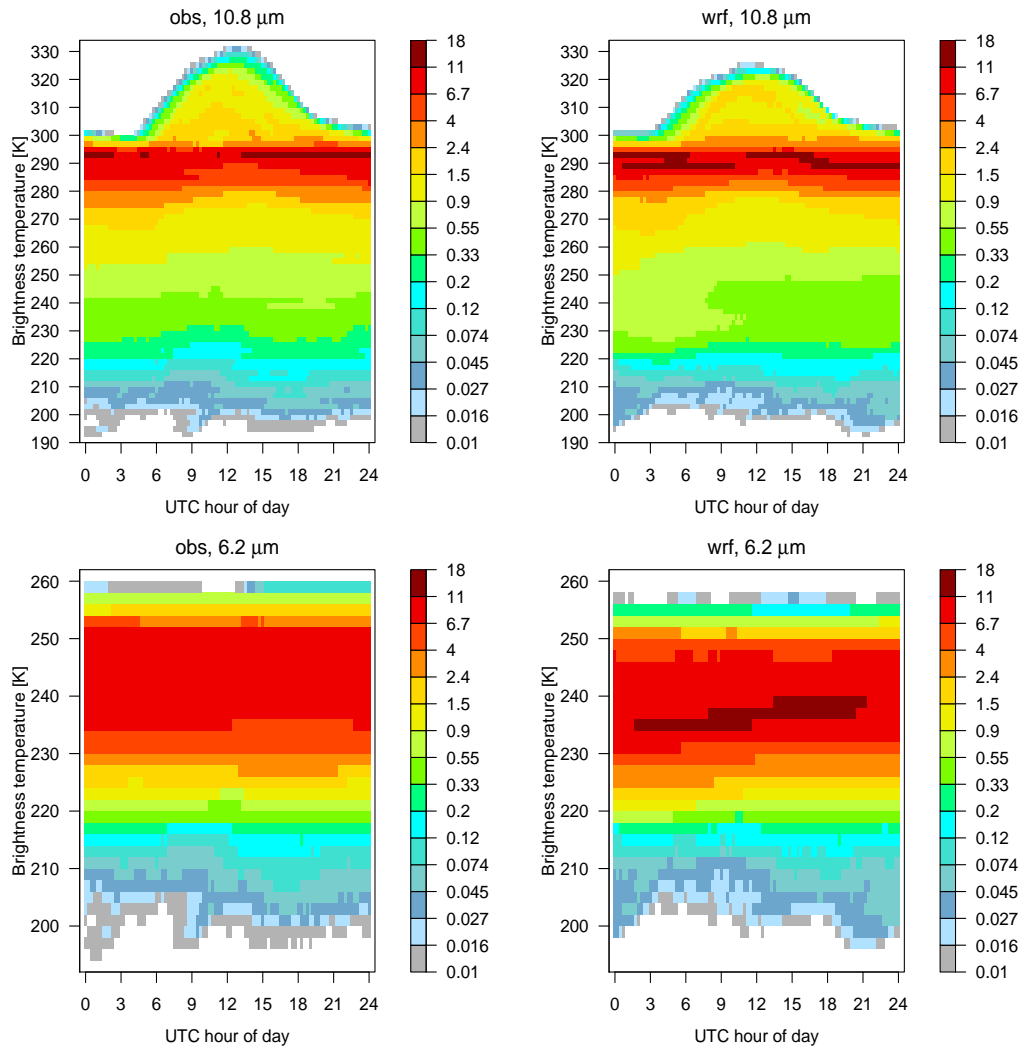
Figure 4: Frequency distribution of brightness temperatures for the IR10.8 (upper row) and WV6.2 (lower row) SEVIRI channels, as a function of the time of day, for observed images (left) and WRF simulated images (right). Statistics are shown for each time step, based on all pixels with a satellite zenith angle less than 70°, within the latitude range of the WRF model. The bin size is 2K.
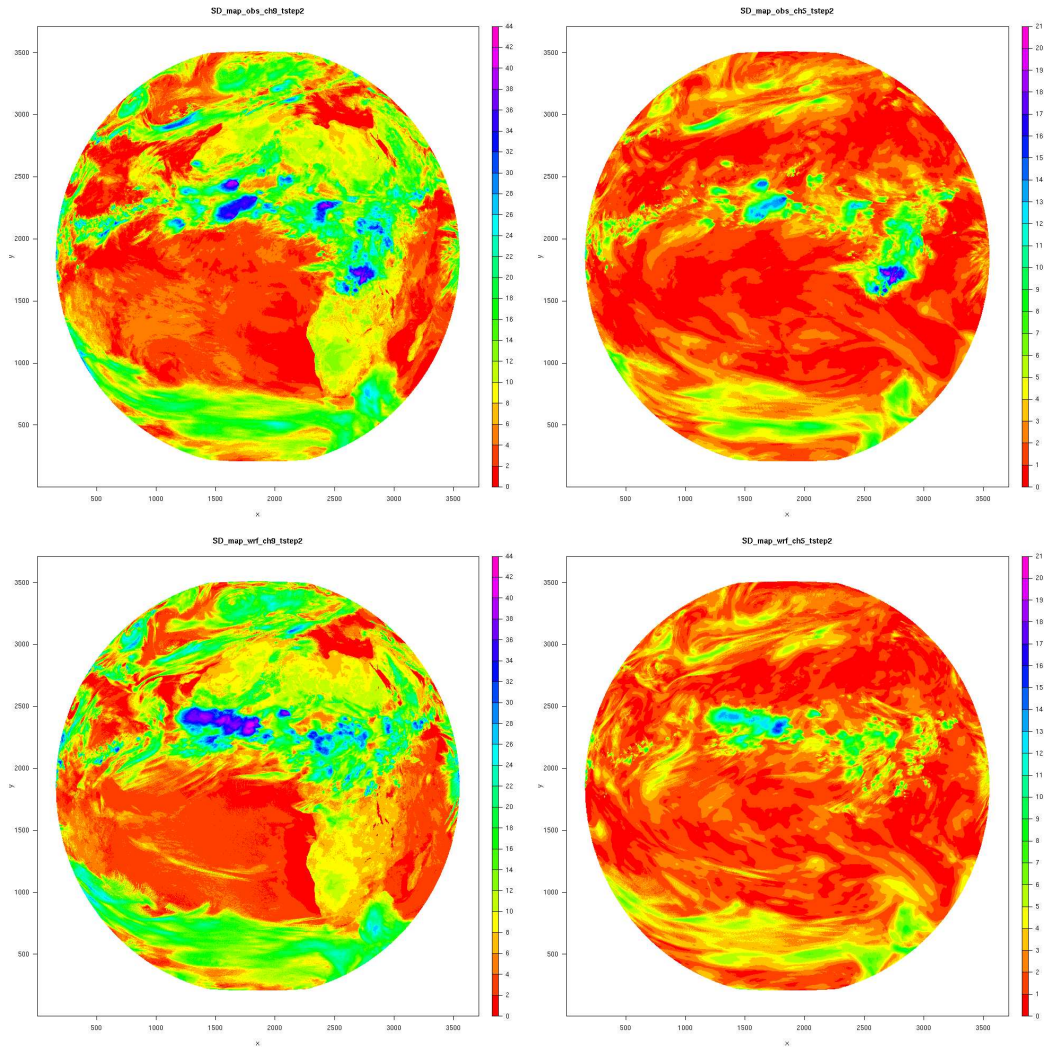
Figure 5: Standard deviation of the time series of BT for each pixel in the WRF / MSG area for: observed images (top) and WRF simulated images (bottom), for SEVIRI channels IR10.8 (left column) and WV6.2 (right column).
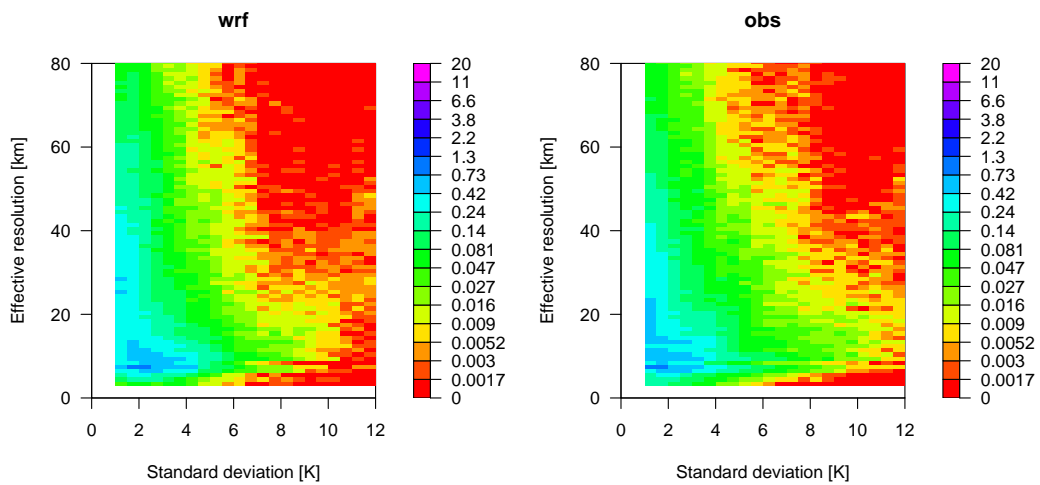
Figure 6: Two-dimensional histograms of the percentage of pixels with a given standard deviation of brightness temperatures/effective resolution for the WV6.2 channel. The WRF simulation is on the left, and the observed distribution on the right.
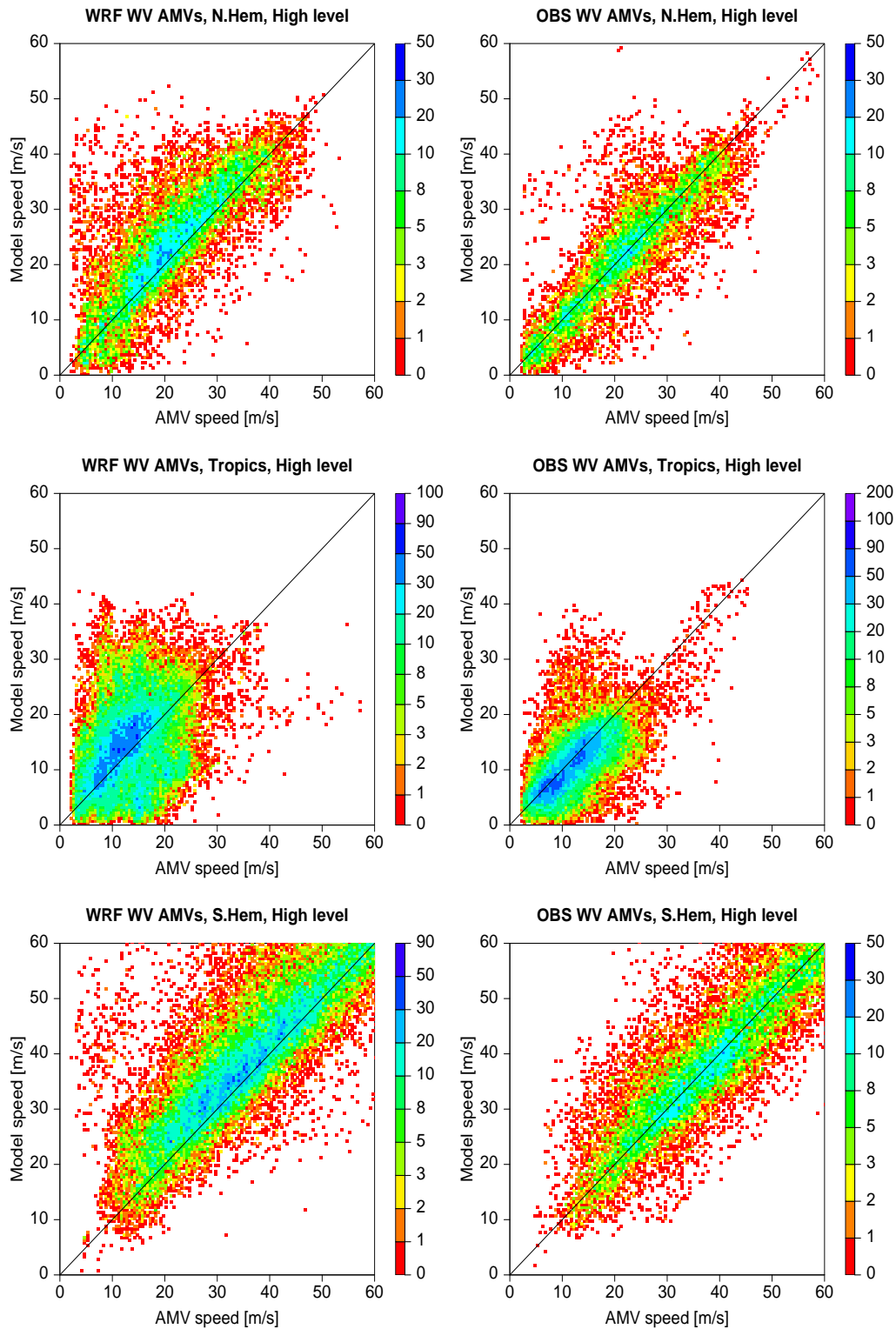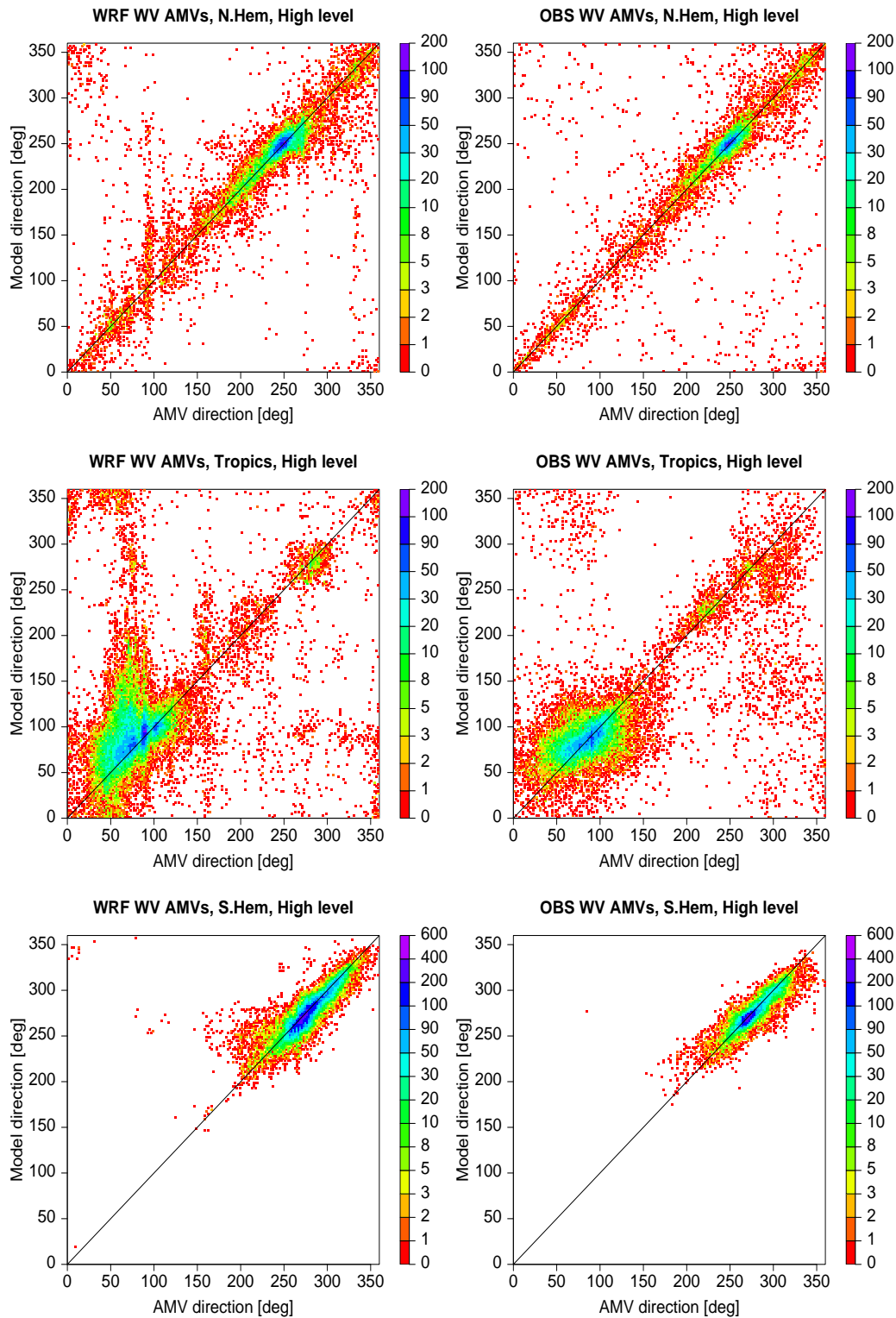
Figure 7: 2D histograms of speed for high-level AMVs derived from WV6.2 images, from WRF simulated imagery (left) and from operations at the time of the study period (right), for northern hemisphere extra-tropics (top), tropics (middle row) and southern hemisphere extra-tropics (bottom). All AMVs are from cloudy tracers. Only AMVs with a model-independent QI > 80% have been selected.

ECMWF

Atmospheric Motion Vectors from model simulations. Part I

Figure 8: *2D histograms of direction for high-level AMVs derived from WV6.2 images, from WRF simulated imagery (left) and from operations at the time of the study period (right), for northern hemisphere extra-tropics (top), tropics (middle row) and southern hemisphere extra-tropics (bottom). All AMVs are from cloudy tracers. Only AMVs with a model-independent QI > 80% have been selected.*

Atmospheric Motion Vectors from model simulations. Part I

ECMWF
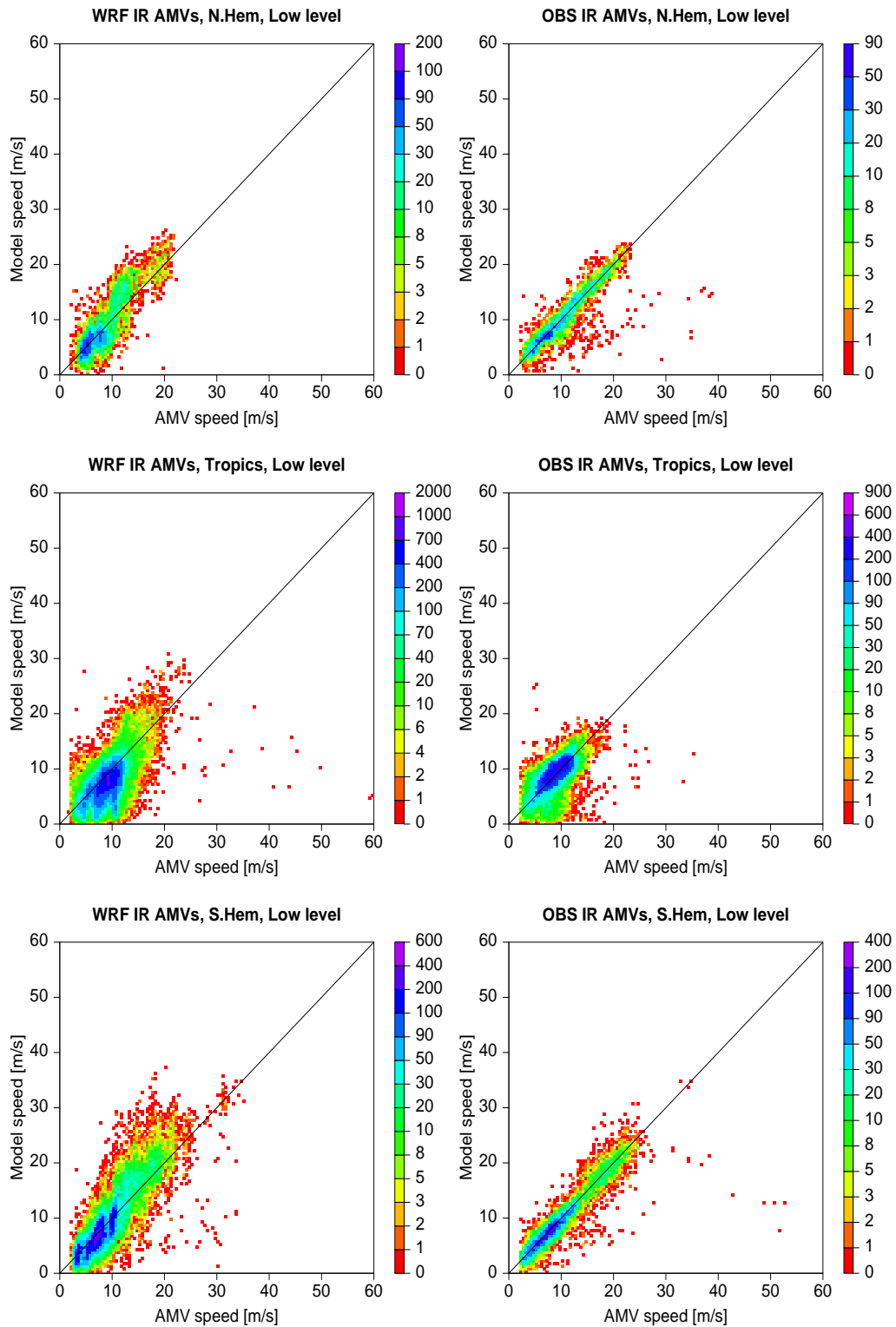
Figure 9: *2D histograms of speed for low-level AMVs derived from IR10.8 images, from WRF simulated imagery (left) and from operations at the time of the study period (right), for northern hemisphere extra-tropics (top row), tropics (middle row) and southern hemisphere extra-tropics (bottom row). Only AMVs with a model-independent QI > 80% have been selected.*
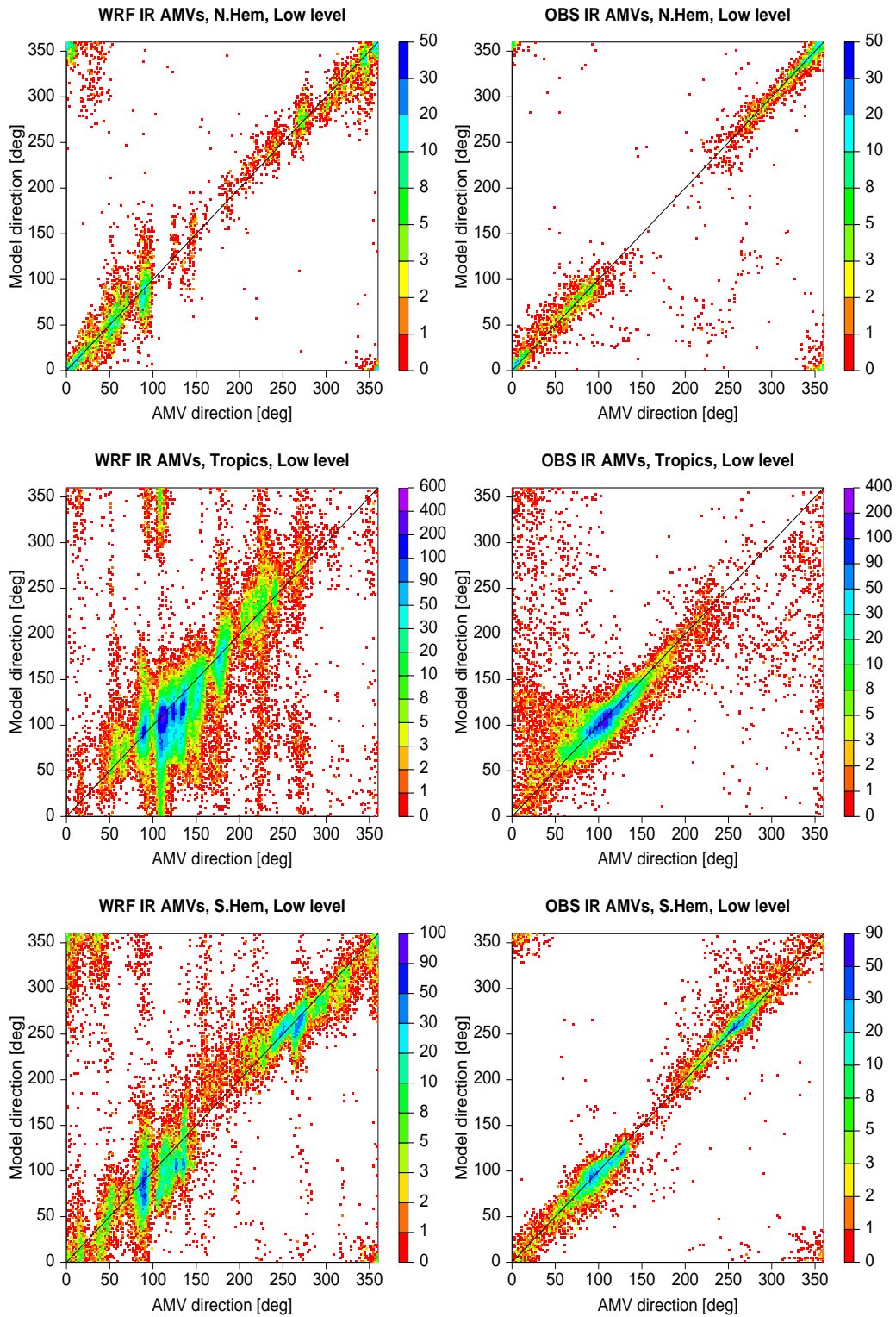
WRF IR AMVs, N.Hem, Low level

OBS IR AMVs, N.Hem, Low level

WRF IR AMVs, Tropics, Low level

OBS IR AMVs, Tropics, Low level

WRF IR AMVs, S.Hem, Low level

OBS IR AMVs, S.Hem, Low level

Figure 10: As in Figure 9, for wind direction.

Atmospheric Motion Vectors from model simulations. Part I

ECMWF
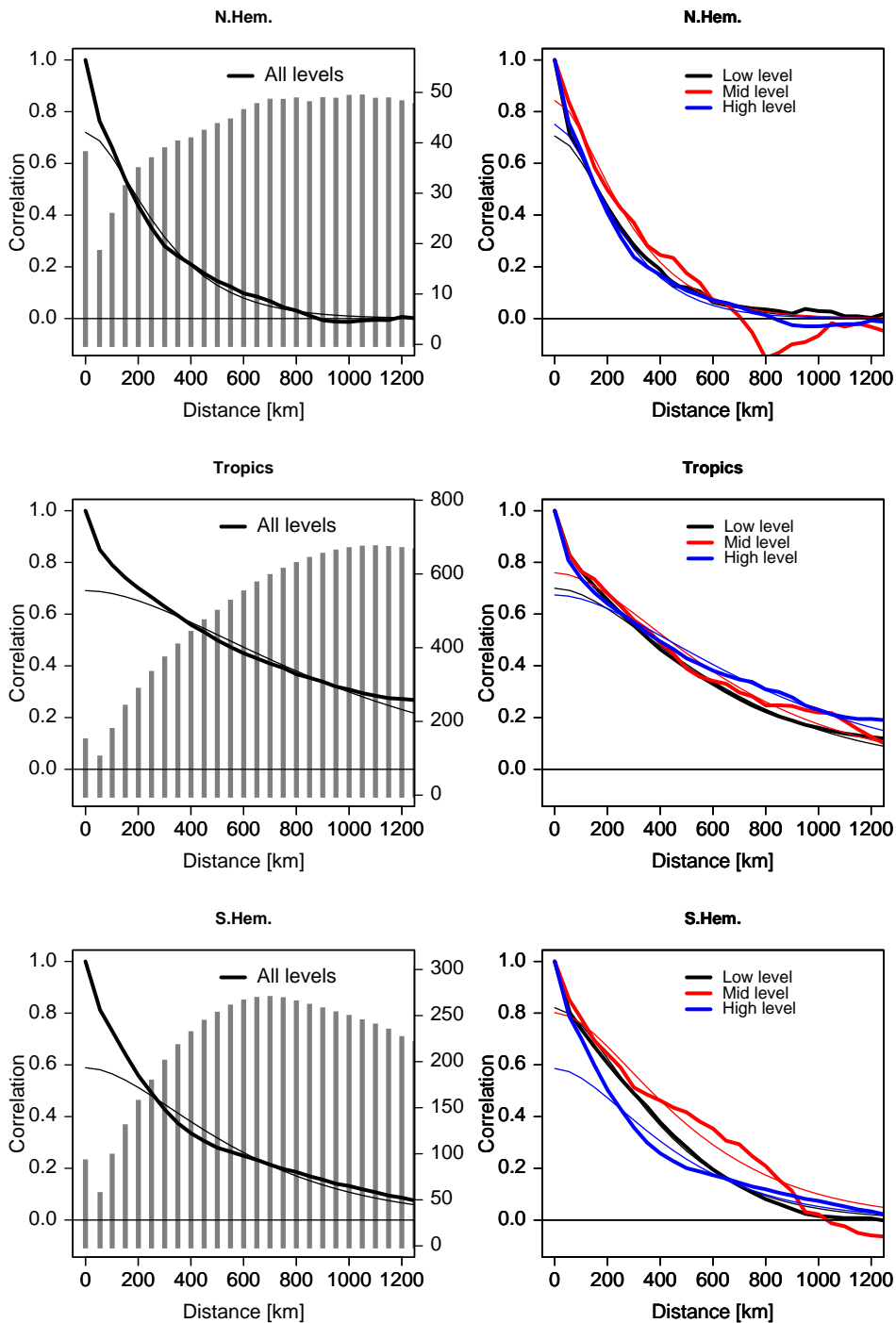
Figure 11: Spatial error correlations for the AMVs derived from the IR imagery of the WRF simulations (thick lines). The left column shows results for all levels combined, whereas the right column shows results separated by layers in the vertical (see legend). The rows show results for the northern hemisphere extra-tropics, tropics, and southern hemisphere extra-tropics, respectively. Also shown are the fits of the SOAR function (thin lines), and, for the left column, the number of AMV pairs used in each distance separation bin as vertical bars (in thousands, see right hand y-axis).
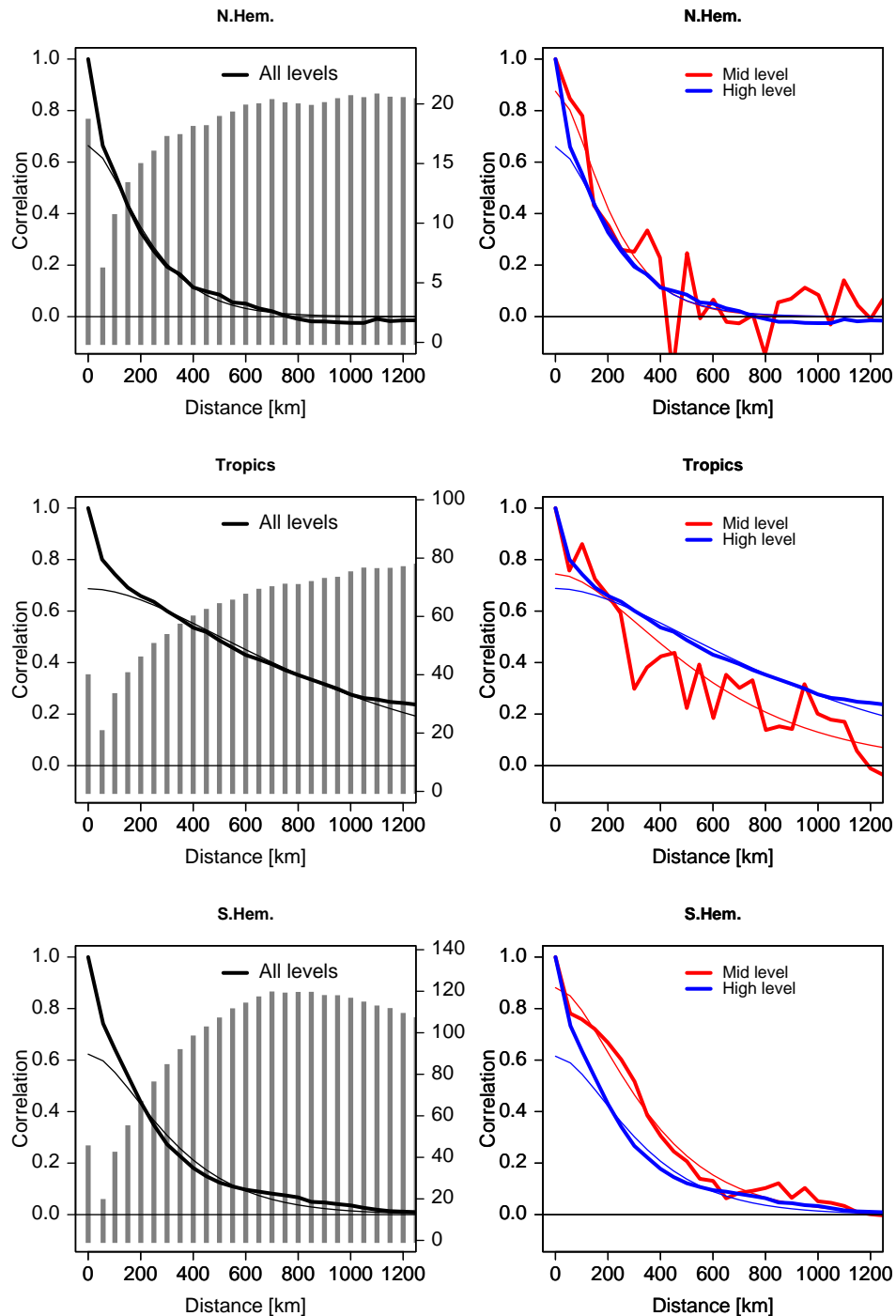
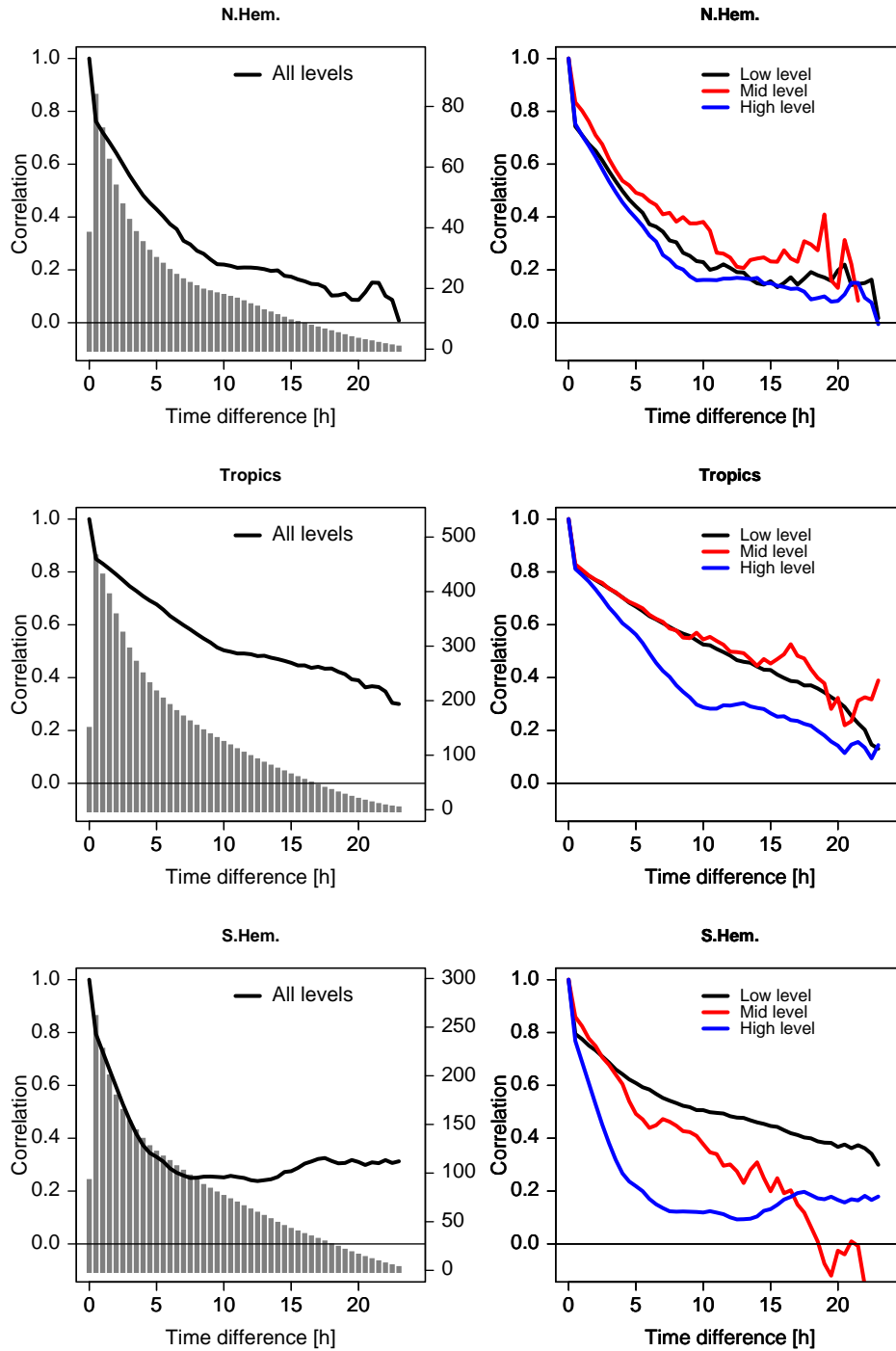*Figure 12: As Fig. 11, but for the AMVs derived from the WV channel.*

Figure 13: As Fig. 11, but for temporal error correlation. No fit to an analytical correlation function is shown here.
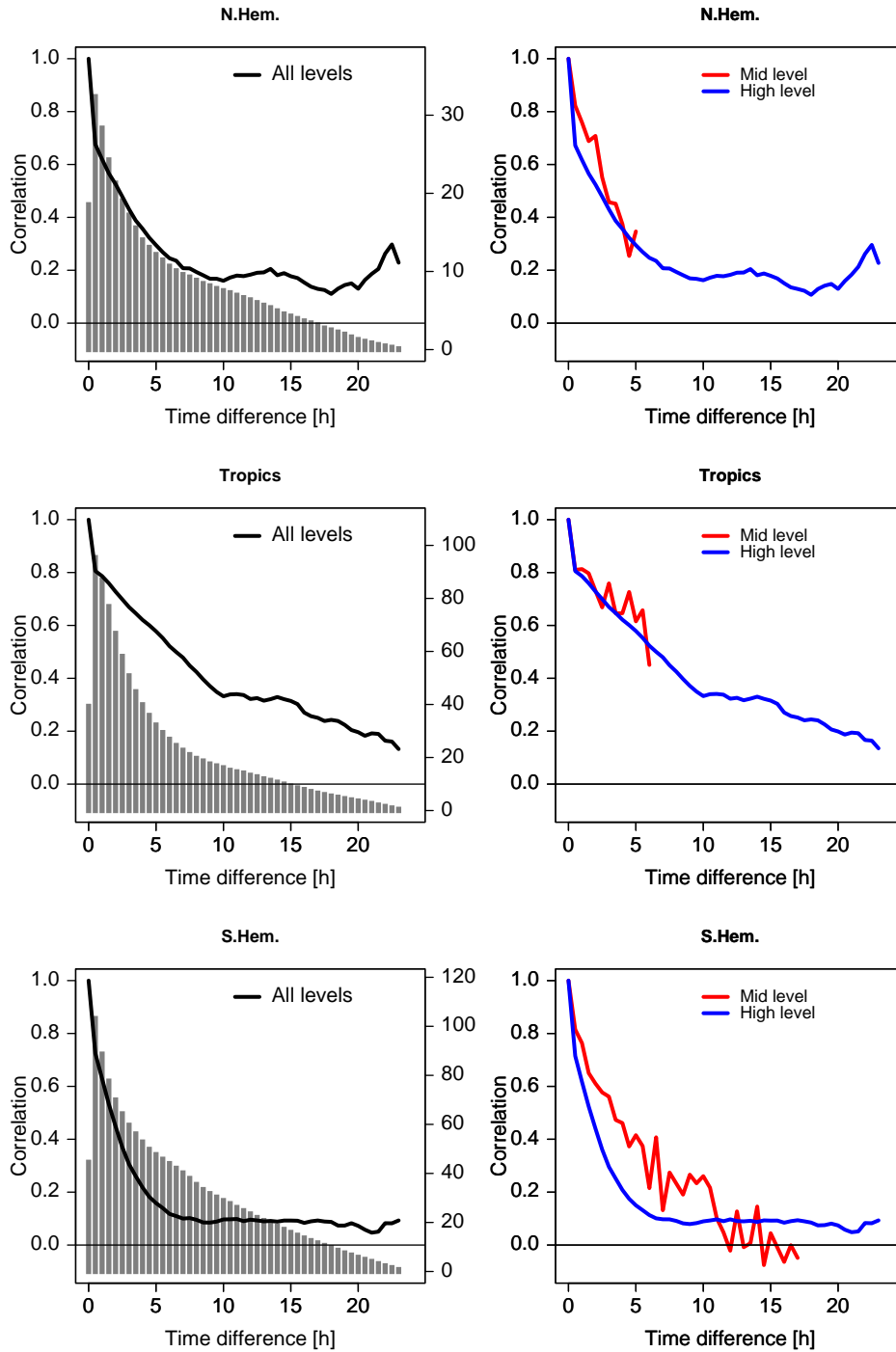
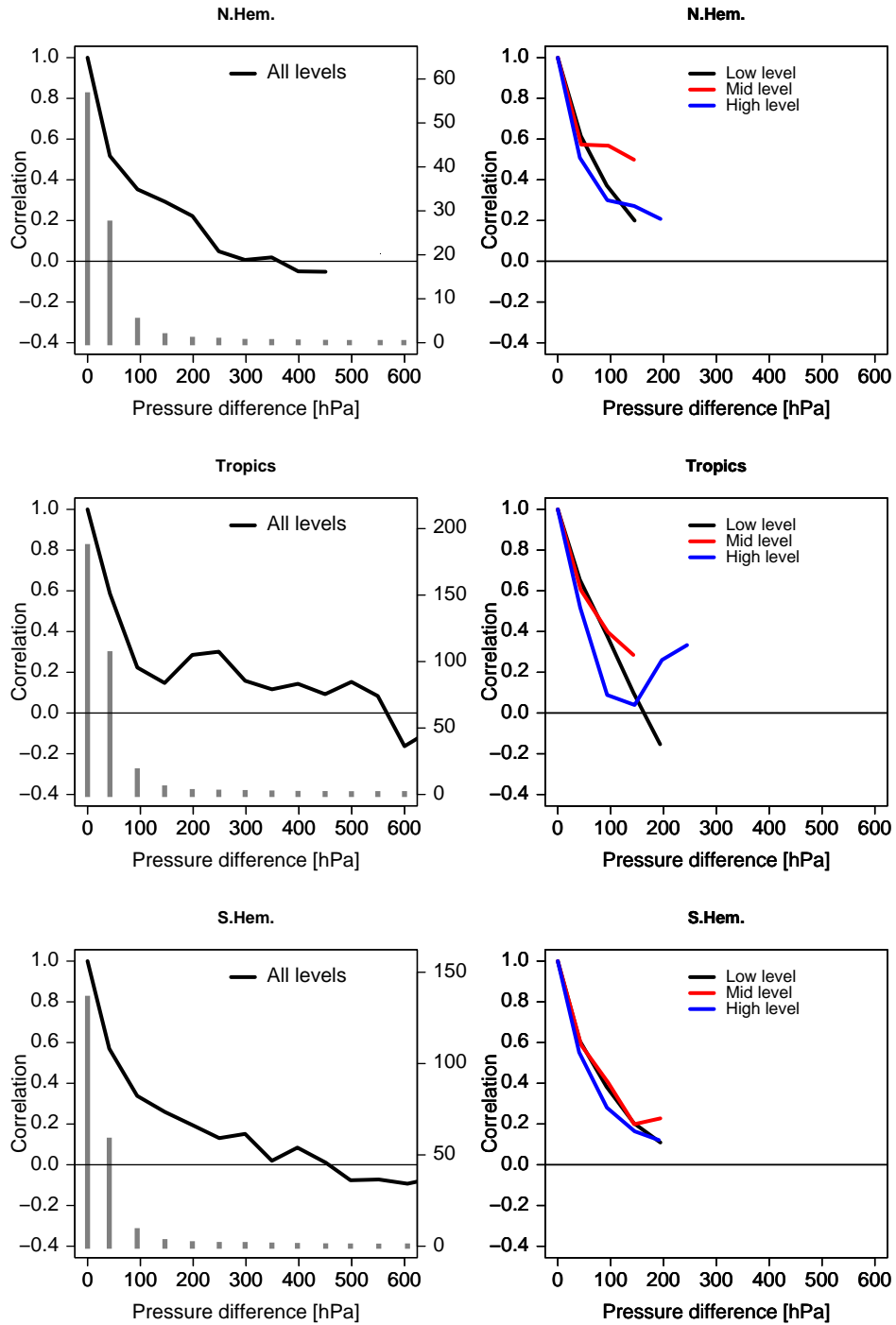Figure 14: As Fig. 13, but for the AMVs derived from the WV channel imagery.

Figure 15: As Fig. 11, but for vertical error correlations for AMVs derived from the IR or the WV channel imagery.